Perez, J., Tobler, D. J., Freeman, H. M., Brown, A. P., Hondow, N. S., van Genuchten, C. M., Benning, L. G. (2021): Arsenic species delay structural ordering during green rust sulfate crystallization from ferrihydrite. - Environmental Science: Nano, 8, 10, 2950-2963.

https://doi.org/10.1039/D1EN00384D

View Article Online
View Journal

Environmental Science Nano

Accepted Manuscript

This article can be cited before page numbers have been issued, to do this please use: J. P. Perez, D. Tobler, H. Freeman, A. P. Brown, N. S. Hondow, C. M. van Genuchten and L. G. G. Benning, *Environ. Sci.: Nano*, 2021, DOI: 10.1039/D1EN00384D.

ROYAL SOCIETY OF CHEMISTRY

rsc.li/es-nano

View Article Online
DOI: 10.1039/D1EN00384D

Environmental significance

Green rust (GR) is a mixed-valence Fe phase that has a high uptake capacity for arsenic (As). However, our understanding of GR formation in As-contaminated environments, as well as the stability of As-bearing GR, is still fragmented. Here, we document how in a system catalyzed by Fe^{2+}, both As(III) and As(V) when sorbed to ferrihydrite inhibits GR sulfate crystallization, affecting structural ordering and phase transformation mechanisms. As(III) exhibited a stronger inhibitory effect (at least eight-fold) on GR sulfate crystallization compared to As(V), and it also increased GR stability and prevented its transformation to magnetite. These results clearly demonstrate how As sorption can increase GR stability, potentially limiting As remobilization in reduced subsurface settings.

DOI: 10.1039/D1EN00384D

Arsenic species delay structural ordering during green rust sulfate crystallization from ferrihydrite†

Jeffrey Paulo H. Perez,*[a,b] Dominique J. Tobler,[c,d] Helen M. Freeman,[e] Andy P. Brown,[e] Nicole S. Hondow,[e] Case M. van Genuchten,[f] Liane G. Benning[a,b]

[a] *Sec. 3.5 Interface Geochemistry, GFZ German Research Center for Geosciences, Telegrafenberg, 14473 Potsdam, Germany. E-mail: jpperez@gfz-potsdam.de*

[b] *Department of Earth Sciences, Freie Universität Berlin, 12249 Berlin, Germany*

[c] *Nano-Science Center, Department of Chemistry, University of Copenhagen, 2100 Copenhagen, Denmark*

[d] *Department of Plant and Environmental Sciences, University of Copenhagen, 1871 Frederiksberg C, Denmark*

[e] *Leeds Electron Microscopy and Spectroscopy Centre (LEMAS), School of Chemical and Process Engineering, University of Leeds, Leeds LS2 9JT, United Kingdom*

[f] *Geological Survey of Denmark and Greenland (GEUS), 1350 Copenhagen, Denmark*

† *Electronic supplementary information (ESI) available.*

View Article Online
DOI: 10.1039/D1EN00384D

Abstract

Green rust (GR) is an Fe(II)-Fe(III)-bearing phase that forms in oxygen-poor and Fe^{2+}-rich subsurface environments where it influences trace element cycling and contaminant dynamics. GR phases have been shown to have high arsenic (As) uptake under anoxic and circum-neutral pH conditions. While geochemical controls on As uptake by GR have been identified, we still lack a fundamental understanding about GR formation in As-contaminated soils and groundwater, as well as the stability of As-bearing GR solids. In this study, we quantified the influence of As(III) and As(V) ($[As]_{initial}$ = 100 µM) on GR sulfate (GR_{SO4}) crystallization during the Fe^{2+}-induced transformation of ferrihydrite (FHY) at pH 8 (As/Fe_{solid} = 0.008, $Fe^{2+}_{(aq)}/Fe(III)_{FHY}$ = 3). We also documented the behavior of mineral-bound As during GR_{SO4} crystallization and its transformation to magnetite. Our results showed that, compared to the As-free system, adsorbed As species delayed FHY transformation to GR_{SO4}. Moreover, As(III) had a stronger inhibitory effect (at least eight-fold) than As(V) on GR_{SO4} crystallization, and reduced structural coherence and ordering in As(III)-bearing GR_{SO4} crystals. During FHY dissolution, we observed an initial release of ~14 µM As(III) into the aqueous phase, but this was quickly adsorbed by newly-formed GR_{SO4} crystals. Mineral-bound As(III) resulted in at least four-fold increase in GR_{SO4} phase stability compared to As(V), and fully prevented its transformation to magnetite even after 720 h. Our results provide new information on the pathways of interaction of common Fe phases exposed to reducing, Fe^{2+}-bearing and As-contaminated fluids and how these affect the structure, morphology and stability of As-bearing GR phases.

View Article Online
DOI: 10.1039/D1EN00384D

1. Introduction

Green rust (GR) is a highly reactive mixed-valence iron-bearing mineral, consisting of alternating positively charged Fe(II)-Fe(III) hydroxide sheets and negatively charged interlayers with anions (e.g., Cl^-, CO_3^{2-}, SO_4^{2-}) and water molecules.[1] GR phases are increasingly being recognized as an important mineral in oxygen-poor, ferruginous (i.e., Fe^{2+}-rich) natural and engineered settings as their reactivity can heavily impact the cycling of Fe and also the distribution and speciation of nutrients and contaminants. GR phases are redox active and nanoparticulate and, thus, have high affinity for toxic metals and metalloids (e.g., As, Cu, Pb, Ni, Zn) in contaminated environments.[2-6]

Arsenic (As) is one of these toxic metal(loid)s and a well-known soil and groundwater contaminant affecting drinking water supplies for up to 220 million people worldwide,[7-9] mostly in South and Southeast Asia. As-contaminated groundwaters in these regions are usually characterized by reducing conditions,[10] and they can contain As concentrations between 10 and 5000 µg L^{-1},[11,12] often exceeding the World Health Organization provisional limit for As in drinking water of 10 µg L^{-1}.[13] In these systems, reduced inorganic As species, arsenite ($H_3As^{III}O_3$), is the dominant As species, while the oxidized, arsenate ($H_3As^{V}O_4$) species is less abundant, and also less mobile and less toxic.[8,14] Various studies have documented that As(III) has a weak sorption affinity to common soil minerals such as iron(III) (oxyhydr)oxides,[15-18] thus keeping the reduced As species in solution and mobile in soils and groundwater. However, we have recently shown that when using an Fe(II)-Fe(III) hydroxide such as green rust sulfate (GR_{SO4}), we could effectively remove both As species, adsorbing up to 160 mg As(III) and 105 mg As(V) per g solid, which is among the highest values reported for common Fe minerals (see Ref. 19 and references therein). This makes GR phases potentially important mineral substrates for As immobilization in reduced environments (e.g., Root et al.[2], Perez et al.[20]).

GR phases commonly form in anoxic natural environments via the Fe^{2+}-induced transformation of metastable Fe(III)-bearing minerals such as ferrihydrite (FHY),[21] with the dissolved Fe^{2+} most often produced by dissimilatory iron-reducing bacteria.[22] The transformation process is initiated by the dissolution of the FHY nanoparticles as a result of Fe(II)-Fe(III) electron transfer at the FHY mineral-

View Article Online
DOI: 10.1039/D1EN00384D

water interface.[21] At low Fe^{2+} concentrations, this results in the precipitation of thermodynamically more stable Fe phases such as lepidocrocite and/or goethite;[23,24] while at high Fe^{2+} concentrations, mixed-valence Fe phases like GR (Fe(II)/Fe(III) ≈ 2-3) and magnetite (Fe(II)/Fe(III) = 0.5) form.[25,26]

While the mechanism of GR formation via Fe^{2+}-induced transformation of FHY is well understood,[25,26] a quantitative assessment of the role of GR in decreasing As mobility and toxicity in reduced, contaminated soils and groundwater is still lacking. Studies that investigated the Fe^{2+}-induced transformation of As-bearing FHY under anoxic and circum-neutral pH conditions at low molar ratios of aqueous Fe^{2+} to the FHY precursor ($Fe^{2+}_{(aq)}/Fe(III)_{FHY}$ ratio = 0.1-2), documented that the mineral end-products either consisted of lepidocrocite and/or goethite.[27,28] We have recently shown that GR with interlayer sulfate (GR_{SO4}) can form together with goethite from As(V)-bearing FHY reacted for 24 h at a $Fe^{2+}_{(aq)}/Fe(III)_{FHY}$ molar ratio of 2,[29] which corresponds to the stoichiometric Fe(II)/Fe(III) ratio of GR_{SO4}.[30,31] Note that with aging, GR_{SO4} eventually dissolved and re-precipitated as goethite because the latter is a more thermodynamically stable Fe phase. Despite these findings, there are still gaps in our understanding of GR formation in the presence of As species under anoxic conditions. For example, the absolute amounts of FHY ($[Fe(III)]_{FHY}$ ≈ 40 mM) and dissolved Fe^{2+} (up to ~80 mM) used in our previous work were relatively high compared to those found in As-affected regions in South and Southeast Asia. In addition, GR was not the dominant mineral phase in all these previous studies, which makes it difficult to evaluate the effect of As on GR crystallization, as well as the fate of As during the early stages of crystallization.

GR phases are, however, thermodynamically less stable compared to other Fe (oxyhydr)oxides,[1] often transforming to magnetite (MGT) via dissolution-reprecipitation pathway in reduced environments.[26] It is therefore important to assess the stability of As-bearing GR phases upon aging to determine whether such mineral transformation can result in As remobilization. To the best of our knowledge, only a few studies examined the prolonged phase stability of As-bearing GR solids under anoxic and circum-neutral pH conditions (Table 1). Wang and co-workers[32] followed the Fe^{2+}-induced transformation of lepidocrocite ($Fe^{2+}_{(aq)}/Fe(III)_{solid}$ = 0.5, As/Fe_{solid} = 0.008-0.04) at pH ~6.6 over

7 days, forming MGT as the transformation end-product and GR chloride (GR_{Cl}) as a transient phase. Their results showed that higher As/Fe_{solid} ratios delayed the transformation of GR_{Cl} to MGT in the system, with As(III) having a greater effect compared to As(V). In contrast, van Genuchten et al.[33] reported that GR carbonate (GR_{CO3}) prepared by Fe(0) electrolysis ($Fe^{2+}_{(aq)}/Fe(III)_{solid}$ = 3) transformed to MGT in the presence of As(III) within one day (As/Fe_{solid} = 0.03), while it took >30 days in the presence of As(V) (As/Fe_{solid} = 0.008). These studies have provided important insights on the effect of As speciation and As/Fe_{solid} ratios on GR stability. However, critical details during the gradual transition from GR to MGT are still missing due to the large gap between sampling time intervals in these studies. For example, these studies lack information on changes in solution chemistry (e.g., [Fe] and [As]) during GR formation and its subsequent transformation to MGT, as well as nanoscale structural information about the resulting As-bearing GR solids.

Table 1. Studies on the transformation of As-bearing GR phases to MGT under anoxic and circum-neutral pH conditions.

Starting GR phase	$Fe^{2+}_{(aq)}/Fe(III)_{solid}$ ratio	Background electrolyte	pH	$[As]_{initial}$ (mM)	As/Fe_{solid} ratio	As oxidation state	MGT formation (d)	Reference
GR_{Cl} (via LP)	0.5	60 mM NaCl	6.6	0.67	0.008	+3	7	Wang et al.[32]
						+5	1	
				3.34	0.04	+3	> 365	
						+5	7	
GR_{CO3}	3	2 mM $NaHCO_3$ + 10 mM NaCl	8.0	0.015	0.007	+3 / +5[a]	1	van Genuchten et al.[33]
				0.06	0.03	+5	> 30	
GR_{SO4}	2.1	Natural GW[b]	7.5	0.08	0.006	+3 / +5[c]	120	Perez et al.[20]
							> 424[d]	
GR_{SO4} (via FHY)	3	100 mM NaCl	8.0	0.1	0.008	+3	> 30	This work
						+5	15	

Note: [a]from partial reduction of initial As(III) with ~25% As(V) in the solid; [b]natural groundwater (GW) with high HCO_3^- (~4.5 mM) and Si (~0.6 mM), see Perez et al.[20] for detailed GW composition; [c]equimolar concentrations in initial As solution; [d]As-bearing GR sample aged at 4 °C

To fill these knowledge gaps, we quantified GR_{SO4} crystallization, as well as its transformation to MGT, during the Fe^{2+}-induced transformation of ferrihydrite ($[Fe(III)]_{FHY}$ ≈ 4 mM). The experiments were carried out in the presence of either As(III) or As(V) ($[As]_{initial}$ = 100 µM) at relevant groundwater conditions (pH ~8, IS = 0.1 M, As/Fe_{solid} = 0.008) over a period of 30 days (720 h). Our main aim was to

View Article Online
DOI: 10.1039/D1EN00384D

examine the influence and fate of As(III) and As(V) on GR_{SO4} crystallization from ferrihydrite under reducing conditions. We evaluated the crystallization and stability of GR over a month-long time scale to address possible remediation scenarios (e.g., *in situ* particle injection) in contaminated aquifers. We therefore used an $Fe^{2+}_{(aq)}/Fe(III)_{FHY}$ of 3 to ensure excess dissolved Fe^{2+} with respect to the GR_{SO4} stoichiometric Fe(II)/Fe(III) of 2 (see Figure S1),[25,34] and carried out experiments under conditions where MGT is the final end-product in an As-free system.[26] We combined aqueous geochemical analysis, powder X-ray diffraction, high-resolution electron microscopy and As K-edge X-ray absorption spectroscopy to determine the structural, morphological and compositional changes in the As-bearing solids as the initial FHY transformed to GR_{SO4}, with a particular focus on the earlier stages of GR crystallization. Our results show that As(III) dramatically stabilizes GR compared to As(V) and particularly to the As-fee system, and inhibits its further transformation to MGT, giving new insights on the role of As on GR_{SO4} crystallization, structure and morphology. Ultimately, we demonstrate with this study the potential role of GR phases in controlling the mobility of As in subsurface environments and its potential use as a highly efficient As remediation mineral substrate.

2. Materials and methods

2.1 General methods

All glass- and plastic-ware were cleaned in 5 M HCl for 24 h, followed by thorough rinsing with Milli-Q water (resistivity ~18.2 MΩ·cm). All chemicals were ACS reagent grade from Sigma-Aldrich and Acros Organics and were used as received. All batch experiments were performed at room temperature inside an anaerobic chamber (97% N_2, 3% H_2, Coy Laboratory Products, Inc.). Stock solutions were prepared inside an anaerobic chamber using Milli-Q water, purged with O_2-free nitrogen for at least 4 h prior to its transfer inside the anaerobic chamber.

2.2 Synthesis of 2-line ferrihydrite

View Article Online
DOI: 10.1039/D1EN00384D

Two-line ferrihydrite (FHY) was synthesized by slowly adding 1 M NaOH to 0.1 M $Fe_2(SO_4)_3 \cdot 5H_2O$ until pH ~7 was reached (following the co-precipitation method described by Cornell and Schwertmann[35]). The resulting FHY suspension was washed through six cycles of centrifugation (10,052*g*, 5 min) and re-dispersion in Milli-Q water to remove excess dissolved ions. The washed FHY suspension was then purged with O_2-free nitrogen for at least 4 h to remove O_2 prior to it being transferred to the anaerobic chamber, and was left to equilibrate with the chamber atmosphere overnight. The total Fe concentration in the FHY suspension was determined by dissolving an aliquot in 0.3 M HNO_3, and then analyzed by flame atomic absorption spectrometry (AAS, Perkin Elmer Analyst 800). Each batch of FHY ($[Fe_{tot}]_{solid}$ ≈ 78 mM) was prepared fresh and used on the day of synthesis.

2.3 Batch experiments and phase identification by X-ray diffraction

Inside the chamber, an aliquot of the degassed FHY suspension (~13.4 mL) was added to a 300-mL perfluoroalkyl (PFA) beaker with a 0.1 M NaCl solution (background electrolyte to match groundwater salinity) containing 100 µM As(III) or As(V) (prepared from $NaAsO_2$ and $Na_2H_2AsO_4 \cdot 7H_2O$ salts, respectively). The As-bearing FHY suspensions ($[Fe(III)_{FHY}]$ ≈ 4.2 mM) were adjusted to pH ~8 using a titrator (Metrohm 785 DMP) with 1 M NaOH. The suspensions were equilibrated for 24 h under constant stirring (350 rpm). After equilibration, the dissolved [As] in the solution was below the limit of detection (< 0.21 µM or 15 µg g^{-1}), as measured by inductively coupled plasma optical emission spectrometry (ICP-OES). Dissolved Fe^{2+} was added by mixing ~7 mL of a 0.45 M $Fe^{II}SO_4$ stock solution to the As-bearing FHY suspension to achieve a total volume of ~250 mL and an $Fe^{2+}_{(aq)}/Fe(III)_{FHY}$ ratio of 3. This $Fe^{2+}_{(aq)}/Fe(III)_{FHY}$ ratio was chosen among the tested ratios in our preliminary As-free Fe^{2+}-induced FHY transformation experiments (no As added; see ESI Text S1 for further details) to ensure that GR_{SO4} formation is favored over goethite (Figure S1), and that the transformation to MGT proceeds gradually.[26] The pH of the suspensions was adjusted to ~8 using a titrator, and this was taken as time "zero". The pH of the suspensions was maintained at 8.0 ± 0.3 throughout the experiments by the addition of either 1 M HCl or NaOH. The reaction mixtures were left under constant stirring (350 rpm),

View Article Online
DOI: 10.1039/D1EN00384D

and at specific time intervals (i.e., 0.08, 0.17, 0.25, 0.5, 1, 2, 4, 8, 24, 48, 96, 168, 360 and 720 h), 10-mL aliquots from the reaction vessels were vacuum filtered through a 0.22-µm polycarbonate membrane filter.

Sub-samples of the filtered solids were immediately prepared for powder X-ray diffraction (XRD) measurements to determine the solid phase composition at each time point by smearing the wet sample paste onto a silicon wafer and allowing it to dry inside the anaerobic chamber. The XRD sample holder was sealed using an X-ray transparent dome with a low oxygen diffusion rate to minimize oxidation/transformation of air-sensitive Fe phases (Bruker Dome, Polytron).[29] XRD patterns were recorded on a Bruker D8 powder diffractometer equipped with a BSI Si(Li) solid detector operating at 40 kV and 40 mA using Cu Kα radiation (λ = 1.5406 Å) with a 0.017° step and a measurement time of 2.5 seconds per step in the 2θ range of Bragg angles of 5° to 70°. The individual XRD patterns were fitted with a pseudo-Voigt function using the HighScorePlus software, and integrated areas of GR_{SO4} (001) and MGT (311) reflections were used to evaluate the degree of crystallinity, termed as degree of reaction (α) from henceforth. The values of α were calculated by normalizing the peak areas according to the equation $\alpha = I_t/I_{max}$, where I_t is the peak area at a given time and I_{max} is the maximum area of the peak, as described in our previous study.[34,36] The degree of reaction was used in this study instead of Rietveld refinement because our objective was to follow the progress of GR and MGT crystallization based on the changes in the peak intensities, not to quantify their relative proportions. This approach also minimizes quantification uncertainties arising from preferred orientation effects which enhance basal plane signals of GR_{SO4}.

The remaining solids were dried inside a desiccator in the anaerobic chamber, and the dried solids were ground and stored in crimped glass vials until used for further characterization. The filtered liquid fractions were acidified using concentrated HNO_3 (Honeywell Fluka™ TraceSELECT™), and stored at 4 °C until the elemental concentrations were analyzed by ICP-OES (Varian 720ES). Detailed information on ICP-OES analysis can be found in our previous work,[19] and detection limits and analytical uncertainties can be found in the Supporting Information (Text S2 and Table S1).

View Article Online
DOI: 10.1039/D1EN00384D

2.4 Material characterization

2.4.1 Transmission electron microscopy

To determine the structure and morphology of the As-bearing precipitates, we cryo-quenched the transformation reactions at specific time intervals (0.25 and 168 h) and analyzed the solids using transmission electron microscopy (TEM). This was done using separate batch transformation experiments with either As(III) or As(V), equivalent to the experiments described above. An aliquot of the reaction suspension was transferred to a headspace crimp vial and loaded in an anaerobic jar (AnaeroJar™ Oxoid™, Thermo Fisher Scientific), and rapidly transferred to the TEM facility. The crimped vial was then opened and the suspension (~3.5 µL) was pipetted onto a continuous amorphous carbon film suspended on a Cu TEM grid. The TEM grid was blotted and plunge frozen into liquid ethane using FEI Vitrobot© markIV (blot force 6). The suspension was exposed to air at 100% humidity for less than 5 s before blotting and plunge freezing. The flash-frozen sample was cryo-transferred to a pre-cooled vacuum drying chamber (~77 K) and the vitreous ice allowed to sublime under high vacuum overnight. This plunge-freeze vacuum-dry method allows us to halt a reaction at a chosen timepoint; it also avoids clustering of particles on the TEM grid as the liquid dispersion is maintained during the plunge freezing process.[37]

Meanwhile, dry powder samples collected at the end of the 720-h reaction in the As(V) system were prepared for TEM by re-suspending in ethanol and sonicating for ~3 min. These suspensions were drop-cast onto a holey amorphous carbon film suspended on a Cu TEM grid. For both sample preparation techniques, the TEM grids were loaded onto a double tilt FEI TEM holder and inserted into the TEM. TEM micrographs and analytical data were collected using an FEI Titan^3 Themis G2 S/TEM operated at 300 kV and equipped with an FEI Super-X 4-detector EDX system, a Gatan One-View CCD and a Gatan Quantum 965 ER imaging filter. Selected area electron diffraction (SAED) patterns were collected using an aperture with an effective diameter of 200 nm at the imaging plane.

View Article Online
DOI: 10.1039/D1EN00384D

2.4.2 Scanning electron microscopy (SEM)

Dry samples were prepared for SEM inside the anaerobic chamber by re-suspending a small aliquot in degassed ethanol and drop-casting directly onto aluminum SEM stubs that were dried inside a desiccator. The stubs were transported to the SEM facility inside an anaerobic jar, loaded onto the sample stage and inserted in the SEM (exposure to air < 1 min). SEM images were acquired using a FEI Quanta 3D FEG SEM operated in high vacuum mode at an acceleration voltage of 10 kV with a secondary electron detector.

2.4.3 As K-edge X-ray absorption spectroscopy

As K-edge X-ray absorption spectroscopy (XAS) data was collected at liquid nitrogen temperatures (~77 K) in transmission and fluorescence modes out to a reciprocal value of 14 $Å^{-1}$ at the BM23 beamline of the European Synchrotron Radiation Facility (ESRF, Grenoble, France).[38] For this, a cryostat was used with helium convection. Fluorescence data were collected using an Si vortex detector. Further information on pellet sample preparation, protocols to prevent oxidation during sample transport and XAS beamline details are described in detail in the Supporting Information (Text S3). All data reduction, linear combination fitting and shell-by-shell fitting of the XAS spectra were performed using the SIXPack software.[39]

3. Results

3.1 Aqueous behavior of Fe^{2+}, SO_4^{2-} and As during the FHY transformation reactions

Solution chemistry analyses of the aqueous ion concentrations during the formation and transformation of GR sulfate (GR_{SO4}), showed that in the As-free system, the dissolved [Fe^{2+}] dropped from ~12.5 mM to ~4.3 mM within the early stages of the reaction (i.e., < 0.08 h; Figure 1a, black circles), accompanied by a decrease in dissolved [SO_4^{2-}] (Figure 1b, black circles). It is noteworthy that full transformation of FHY to GR_{SO4} (stoichiometric Fe(II)/Fe(III) ratio = 2) would require 8 mM Fe^{2+}, leaving a 4 mM Fe^{2+} excess in solution. These changes in solution chemistry coincided with a color

change of the suspension from reddish-brown to dark blue-green. The dissolved [Fe^{2+}] and [SO_4^{2-}] remained fairly constant up until 8 h, but started to increase significantly after 24 h, with the dissolved [Fe^{2+}] released in the solution reaching a maximum of ~7.5 mM at the end of the 720-h reaction. This extensive Fe^{2+} release in solution between 24 and 720 h occurred with a color change of the suspension from blue-green to black.

In the presence of As(III), the dissolved [Fe^{2+}] and [SO_4^{2-}] also remained constant in the early stages of GR_{SO4} crystallization (≤8 h) (Figure 1a and 1b, red squares). The dissolved [Fe^{2+}] was ~4 mM (i.e., expected $[Fe^{2+}]_{aq}$ for stoichiometric GR_{SO4}) up until 168 h (7 d), but then increased up to ~5.8 mM towards the end of the experiment (720 h). Meanwhile, the dissolved [SO_4^{2-}] increased after 360 h (15 d), coinciding with the significant Fe^{2+} release in the solution. Although, Fe^{2+} and SO_4^{2-} were both released in the solution, the color of the suspensions remained dark blue green until the end of the experiment. More importantly, ~13.4% of the mineral-bound As(III) ($[As]_{initial}$ ≈ 100 µM) was released into the solution within the first 0.5 h of the reaction (Figure 1c, red squares), and then gradually increased, reaching a maximum of ~14.3 µM at the end of 8 h. Afterwards, dissolved [As] decreased dramatically resulting in 99.5% removal of the initial As(III) after 720 h.

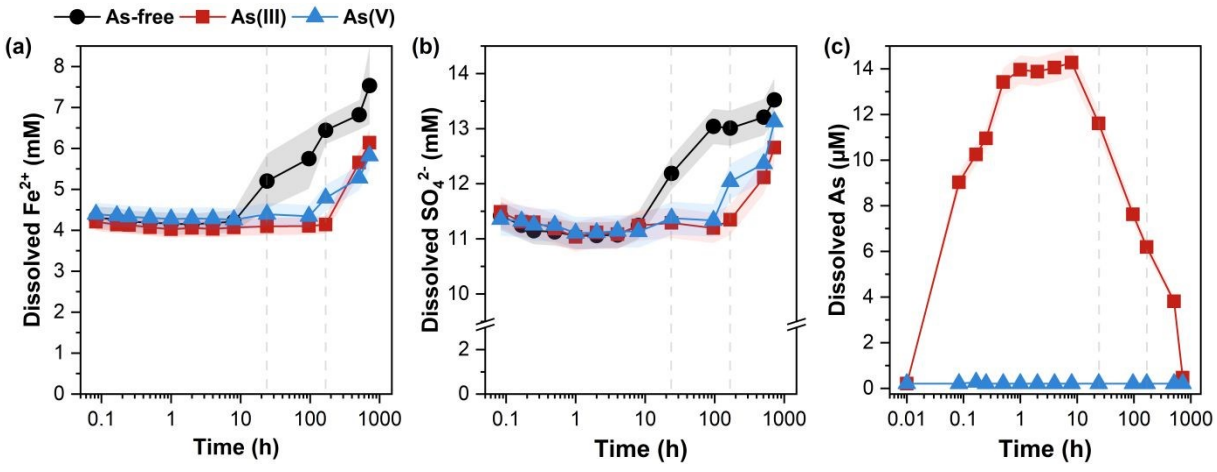

Figure 1. Changes in concentration of dissolved (a) Fe^{2+}, (b) SO_4^{2-} and (c) As over 720 h (30 d) of reaction in the As-free system (black circles), As(III) system (red squares) and As(V) system (blue triangles). The dashed lines mark the sampling times of 24 h and 168 h (7 d). Lightly shaded regions represent analytical uncertainty (<5% relative) based on replicate measurements of QC solutions analyzed together with the samples (Table S1).

In the system where As(V) was present, the behavior of the dissolved [Fe^{2+}] and [SO_4^{2-}] was similar to observations in the As(III) system (Figure 1a and 1b, blue triangles). However, the onset of significant Fe^{2+} and SO_4^{2-} release in the solution happened at 168 h (7 d), which is earlier compared to the As(III) system (360 h). Despite this, the maximum dissolved [Fe^{2+}] at the end of the reaction (~5.8 mM) was still comparable to the As(III) system. This observed Fe^{2+} and SO_4^{2-} release in the later stages of the reaction also coincided with a color change of the suspension from dark-blue green to black. We did not observe any As release in the solution (Figure 1c, blue triangles) contrary to the As(III) system. This could suggest that the release and re-adsorption of As(V) happened quickly, or that minor As(V) was released but was below our instrumental limits (LOD: < 0.21 µM; see Text S2 for more details).

3.2 Evolution of solid phase composition during the FHY transformation reactions

In the As-free system, GR_{SO4} rapidly formed within the first 0.08 h (5 min) after Fe^{2+} addition to the FHY suspension, as evidenced by the appearance of GR_{SO4} basal reflections (00ℓ) in the XRD data (Figure 2a). These GR_{SO4} peaks continued to increase in intensity until they reached a maximum at 24 h (Figure 2a, filled symbols). Once the maximum intensity was reached, the GR_{SO4} peaks started to decrease in intensity, which coincided with the growth of the (311) peak of magnetite (MGT) (Figure 2b, hollow symbols). This change in phase composition from GR_{SO4} to MGT also occurred simultaneously with the rapid increase of dissolved [Fe^{2+}] and [SO_4^{2+}] in the solution (Figure 1a and 1b) starting at 24 h. MGT was the sole crystalline phase at the end of the 720-h reaction based on the XRD data.

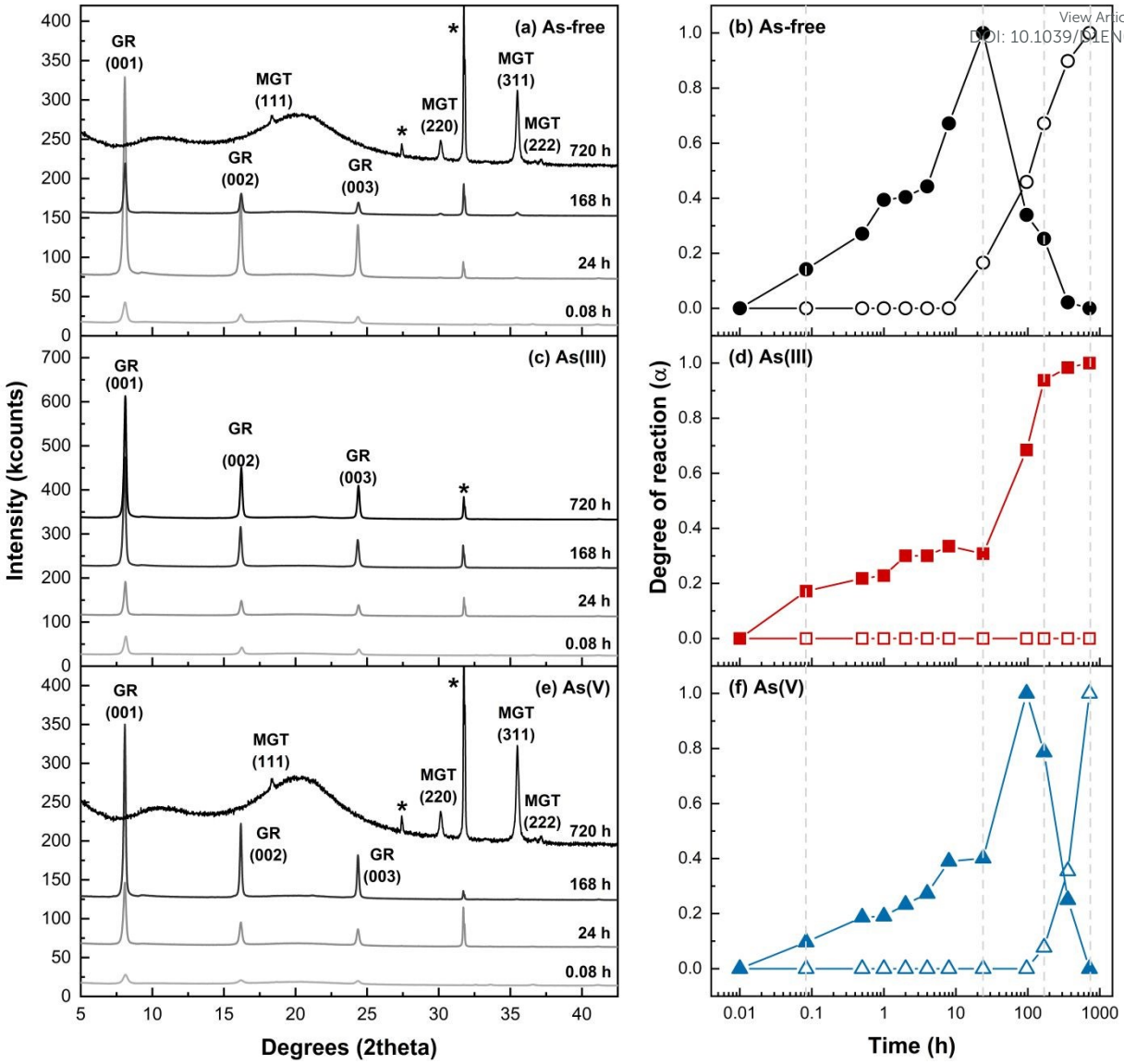

Figure 2. (Left) Powder X-ray diffraction (XRD) patterns of solids collected at different elapsed times, and (right) degree of reaction (α) GR_{SO4} (filled symbols) and MGT (hollow symbols) during the Fe^{2+}-induced transformation of FHY: (a,b) As-free, (c-d) As(III) and (e,f) As(V). The dashed lines (right) mark the sampling times of 0.08 h, 24 h, 168 h (7 d) and 720 h (30 d) of the presented XRD patterns (left). Note that the intensity of the XRD pattern of solids after 720 h in the (d) As-free and (f) As(V) systems were multiplied by 15 and 20, respectively. The amorphous humps at ~11° and ~20° 2theta come from the XRD sample holder and '*' indicates halite (NaCl). The complete XRD patterns for all experimental samples can be found in the Supporting Information (Figure S2-S4).

In the As(III) system, GR_{SO4} was also detected by XRD (Figure 2c) within 0.08 h of the FHY transformation reaction. However, the growth of GR_{SO4} peaks was slower compared to the As-free system (Figure 2d, filled symbols), and peak intensities only started to increase substantially after 24 h. It is noteworthy that rapid growth of GR_{SO4} peaks coincided with the uptake of the dissolved As(III),

which was released at the start of the FHY transformation (Figure 1c). The highest GR_{SO4} peak intensity was observed at 720 h (and could have possibly increased further if monitored longer), but ~94% of this peak intensity was already reached at 168 h (7 d). This suggests that GR_{SO4} crystallization considerably slowed down after 168 h. The slow growth of the GR_{SO4} peaks towards the end of the experiment also overlapped with the release of dissolved Fe^{2+} and SO_4^{2-} release into the solution (Figure 1a and 1b). MGT was not detected in the XRD patterns throughout the transformation reaction. Given that the highest GR_{SO4} peak intensity was only reached at 720 h in the As(III) system (or possibly even later), this shows that GR_{SO4} crystallization was severely inhibited compared to the As-free system (by at least 30-times).

In the As(V) system, the growth of the GR_{SO4} peaks (Figure 2e and 2f, filled symbols) from FHY was similarly slow as in the As(III) system during the early stages of the reaction (< 24 h). The GR_{SO4} peaks reached their highest intensity at 96 h (4 d), which was four times slower compared to the As-free system, and then started to decline until they completely disappeared at the end of 720 h. The decrease of the GR_{SO4} peaks was mirrored by the growth of the MGT (311) peak starting at 96 h (Figure 2f, hollow symbols), as well as the increase of dissolved Fe^{2+} and SO_4^{2-} concentrations in the solution (Figure 1a and 1b). After 720 h, MGT was the only Fe crystalline phase identified by XRD analysis of the solids.

3.3 Nano- and molecular-scale characterization of As-bearing solids

3.3.1 Structure and morphology of As-bearing GR_{SO4}

In the As-free system, our XRD data (Figure 2a) indicated that GR_{SO4} formed in the early stages of FHY transformation. The SEM image of the solids collected after 1 h of reaction revealed thin well-defined hexagonal plates (Figure 3a), ranging in width from 500 nm to 1 µm, which is the expected and characteristic morphology of GR_{SO4} particles.[20,34] After 168 h (7 d), the solids were dominated by equiaxed nanoparticles (~50-100 nm clusters; Figure 3b), identified as MGT by our XRD data (Figure 2a), closely associated with the GR_{SO4} plates.

View Article Online
DOI: 10.1039/D1EN00384D

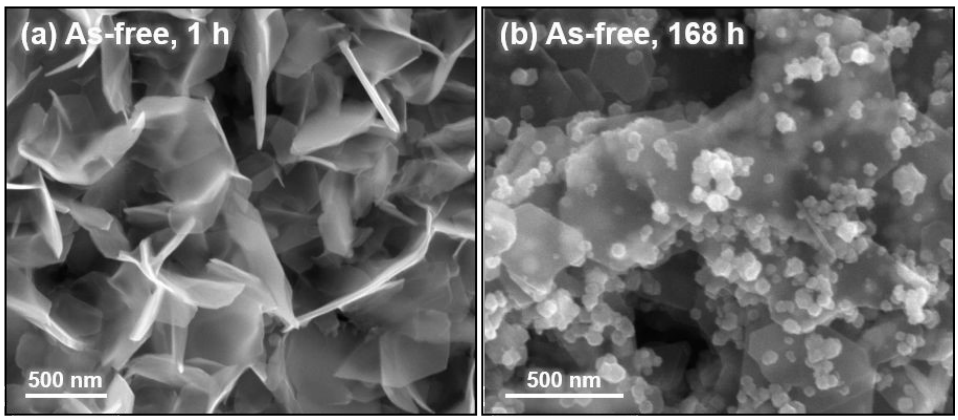

Figure 3. SEM images of the transformation products of FHY in the As-free system: (a) Micron-sized thin hexagonal GR_{SO4} plates after 1 h of reaction; and (b) MGT nanoparticles (50-100 nm clusters) on the surface of GR_{SO4} plates after 168 h (7 d) of reaction.

In the As(III) and As(V) systems, our XRD data (Figure 2c and 2e) revealed that GR_{SO4} particles formed quickly within 0.08 h, although they took longer to reach maximum peak intensity compared to the As-free system. To determine if the As species affected the structure and morphology of the GR_{SO4} precipitates formed at the early stages of the reaction, we cryo-quenched the reaction after 0.25 h (15 min) of reaction, and analyzed the obtained solids by TEM (Figure 4 and 5). It is important to note that the earliest sampling time possible for the cryo-quenched samples was 0.25 h (instead of 0.08 h) due to logistical concerns (i.e., sample transfer from anaerobic chamber to TEM facility).

In the As(III)-reacted solids, two distinct morphologies were observed: (i) micron-sized thin hexagonal plates (Figure 4a) and (ii) thread-like structures (ca. 50 nm in length; Figure 4c). The thin hexagonal plates were confirmed to be GR_{SO4} based on the distinct hexagonal pattern of the (300) and (330) lattice spacings in the fast Fourier transform (FTT; Figure 4a inset) pattern and the measured basal (001) distance of ~11 Å between the GR_{SO4} sheets (Figure 4b). Regarding the thread-like structures, we did not observe lattice fringes, or distinct spots in the FFT or electron diffraction patterns – only strong contrast bands (Figure 4d). This suggests that these thread-like structures might be either poorly crystalline phases, or slightly thicker folded edges of platelets.

View Article Online
DOI: 10.1039/D1EN00384D

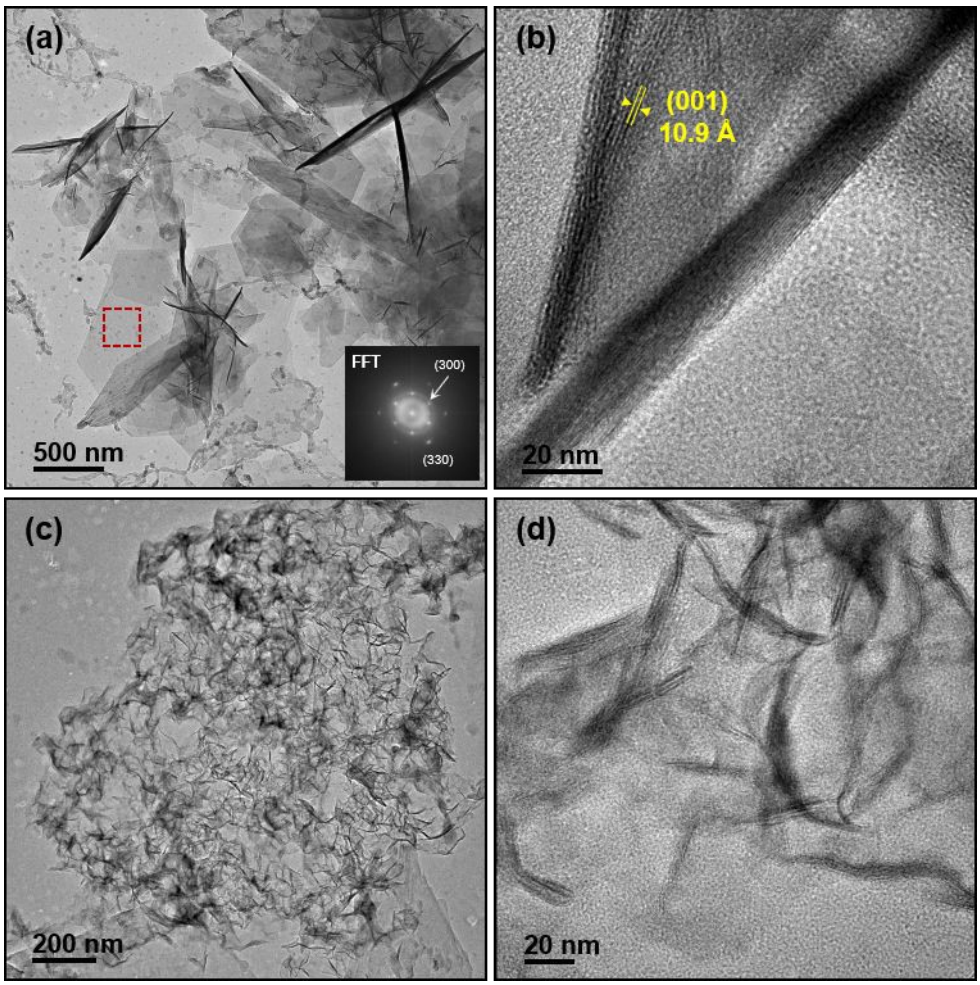

Figure 4. TEM image of the cryo-quenched As(III)-bearing precipitates after 0.25 h (15 min) of reaction: (a) thin micron-sized hexagonal GR_{SO4} plates, as confirmed by the (300) and (330) lattice spacings in the FFT pattern (inset) from the red marked area and observed when the plates are normal to the electron beam (i.e., oriented [001]), and (b) lattice fringes for GR_{SO4} (001) basal spacing when oriented along [300]; and (c-d) thread-like structures (ca. 50 nm in length).

TEM images of the As(V)-reacted solids also exhibited the two distinct morphologies as observed for As(III)-reacted solids, i.e., micron-sized thin hexagonal GR_{SO4} plates (Figure 5a) and thread-like structures (Figure 5b). At higher magnification, lighter contrast nano-sized platelets (ca. 50 nm in diameter) were also found closely associated with the darker contrast thread-like structures (Figure 5c). The FFT pattern from the marked area in Figure 5c, containing both nano-sized platelets and thread-like structures, showed rings with atomic spacing values of 2.77 and 1.60 Å corresponding to GR_{SO4} (300) and (330) lattice planes. Moreover, high resolution TEM (HRTEM) imaging of the nano-sized platelet (Figure 5d) also revealed lattice fringes with the same in-plane atomic spacing values for

View Article Online
DOI: 10.1039/D1EN00384D

(300) and (330) lattice planes. These, therefore, confirm the presence of both nano-sized platelets and thread-like structures of GR_{SO4} oriented along the [001] and [300] axes, respectively.

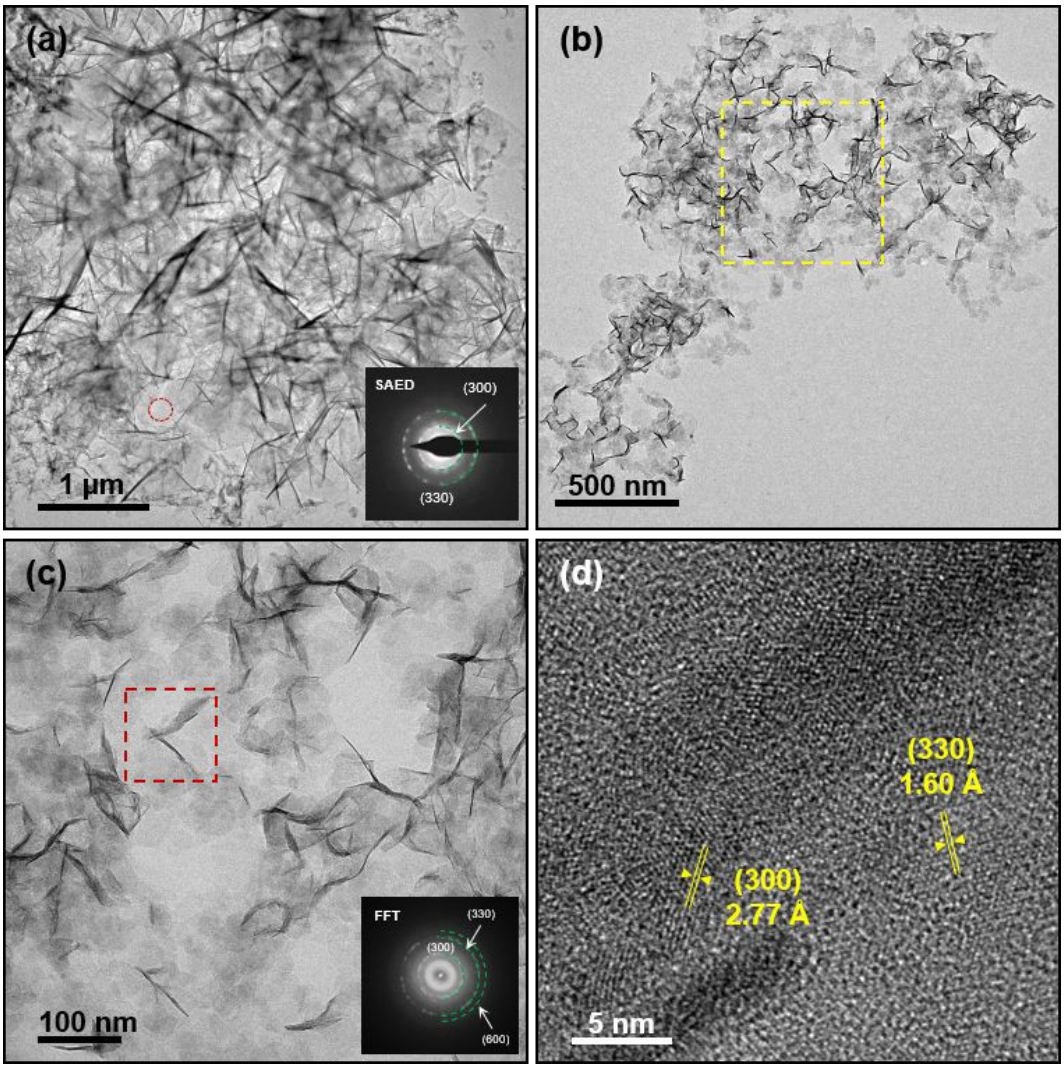

Figure 5. TEM image of the cryo-quenched As(V)-bearing precipitates after 15 min of reaction: (a) thin micron-sized hexagonal GR_{SO4} plates with the selected area electron diffraction (SAED) pattern (inset) from the red marked area; and (b) nano-sized GR_{SO4} platelets. (c) Higher magnification TEM image of the yellow marked area in (b), showing GR_{SO4} platelets oriented along the [001] axis (i.e., lighter contrast nano-sized platelets) and [300] axis (i.e., darker contrast thread-like structures). FFT pattern (inset) of the red marked area in (c) shows characteristic in-plane GR_{SO4} lattice planes. (d) High resolution TEM of the red marked area in (c) with atomic spacing values matching the GR_{SO4} (300) and (330) lattice planes.

We also acquired TEM images of the As-bearing solids after 168 h (i.e., when major changes in solution chemistry and solid phase composition were observed) to determine whether there were

View Article Online
DOI: 10.1039/D1EN00384D

substantial changes in the structure and morphology of the GR_{SO4} particles (Figure 6). In the case of the As(III)-bearing GR_{SO4}, the majority of the particles consisted of micron-sized hexagonal plates (Figure 6a). The lighter contrast of the As(III)-bearing GR_{SO4} particles suggest that the plates are very thin, almost comparable to the 0.25-h reacted solids (Figure 4a). Nano-sized GR_{SO4} platelets were still present in the collected solids (Figure S6a) but less abundant compared to those found after 0.25 h of reaction (Figure 4c). The HRTEM image of the single GR_{SO4} particle in Figure 5a revealed lighter contrast patches with poorer crystallinity (Figure 5b; a few indicated by black arrows), as evidenced by diffuse spots in the FFT pattern (Figure 5b inset). These poorly crystalline patches have been previously observed in naturally occurring GR_{SO4} particles with a high content of Si, which is a structural analogue of As(III).[4,5]

The As(V)-bearing GR_{SO4} particles reacted for 168 h also exhibited morphologies dominated by micron-sized hexagonal plates (Figure 6c), closely associated with minor amounts of nano-sized platelets (also Figure S5b). It is worth noting that these micron-sized plates were thicker (i.e., darker contrast) than those of the As(III)-bearing GR_{SO4} (Figure 6a), and they exhibited dissolution features at the crystal edges (Figure 6c, white arrows). In addition, the nano-sized platelets were less abundant in the As(V)-amended experiment in comparison to As(III). The lighter contrast patches observed in the As(III)-bearing GR_{SO4} plates (Figure 6b) were also absent in the HRTEM image of the As(V)-bearing GR_{SO4} (Figure 6d); instead, several nanocrystalline domains (dark contrast spots) can be seen in the HRTEM (Fig 5d). Moreover, the spots in the FFT pattern (Figure 5d inset) corresponding to the in-plane lattice planes were also sharp and distinct, indicating a more coherent structure compared to that of As(III)-bearing GR_{SO4}.

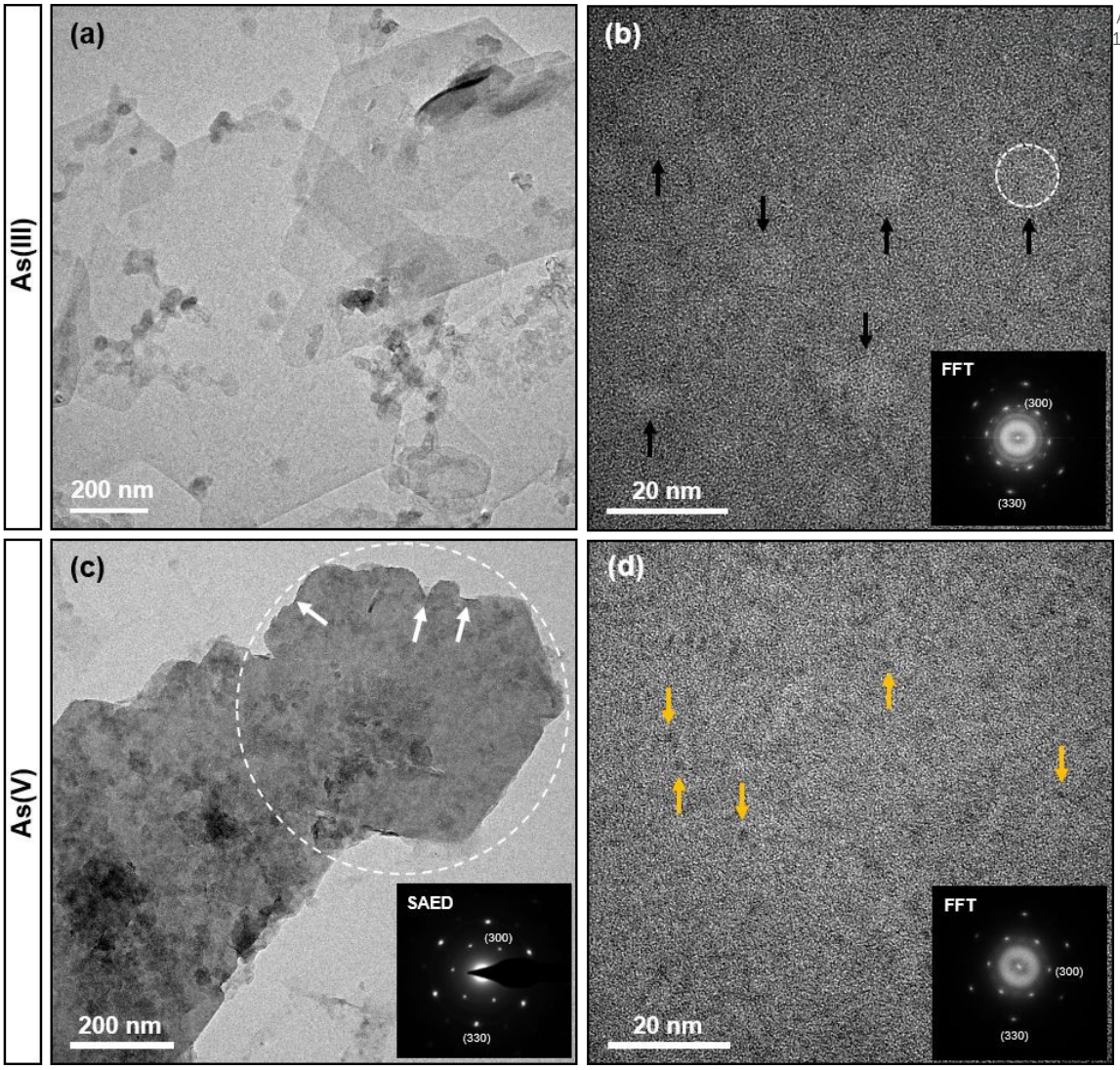

Figure 6. TEM images of the cryo-quenched As(III)- and As(V)-bearing solids after 168 h (7 d) of reaction: (a) As(III)-bearing GR_{SO4} with very thin hexagonal plate morphologies with a few nano-sized platelets. (b) HRTEM image of a single As(III)-bearing GR_{SO4} plate, revealing light patches with very poor crystallinity (black arrows), with the corresponding FFT pattern in the inset. (c) As(V)-bearing GR_{SO4} hexagonal plates exhibiting dissolution features (white arrows) at the crystal edges with the accompanying SAED pattern (inset) collected from the dashed circle. (d) HRTEM image of a single As(V)-bearing GR_{SO4} plate with nanocrystalline domains (i.e., dark contrast spots), a few indicated by yellow arrows, with the corresponding FFT pattern in the inset.

3.3.2 Local structure, composition and morphology of As(V)-bearing MGT end-product

The XRD data of As(V) system (Figure 2e) indicated that MGT was the only crystalline Fe phase found in the solids at the end of the 720 h of reaction. The As(V)-bearing MGT solids were then analyzed by TEM to examine their structure, morphology and composition. The TEM images of the MGT samples (Figure 7 and S6) revealed two distinct morphologies: (1) faceted (ca. 20-50 nm in size; Figure 7a) and

View Article Online
DOI: 10.1039/D1EN00384D

(2) round nanoparticles (ca. 5-10 nm in diameter; Figure 7b). These MGT nanoparticles were enriched with As in the associated EDX spectrum (Figure S7). HAADF-STEM imaging (Figure 7d) coupled with EDX mapping (Figure 7e) revealed that As(V) was homogeneously distributed throughout the faceted and round MGT nanoparticles.

To examine the local structure and As bonding environment, we collected As K-edge X-ray absorption spectroscopy (XAS) data of the As(V)-bearing MGT solids after 720 of reaction. The As K-edge extended X-ray absorption fine structure (EXAFS) spectrum taken from the As(V)-bearing MGT solids (Figure 6f) was characterized by prominent shoulders in its second and third oscillations at 6.8 and 10.8 $Å^{-1}$, respectively. There was also a distinct beat feature at 6.1 $Å^{-1}$. These features are similar to the characteristic EXAFS features of an As(V)-substituted MGT (Figure 7f),[33,40] suggesting similar As coordination environments. Finally, the local bonding environment of As in the MGT solids was derived from shell-by-shell fits of the As K-edge EXAFs spectra (Figure 7h). The fitting results and statistics are shown in Table 2. The first-neighbor contribution to the EXAFS fit was consistent with the As-O atomic correlation for tetrahedral AsO_4 with a coordination number (CN) of ~4 and an interatomic distance of 1.70 ± 0.01 Å.[41] The second-neighbor contribution could not be fitted with a single As-Fe path corresponding to As(V) adsorbed onto MGT in a binuclear corner-sharing (^{2}C) geometry ($CN_{As\text{-}Fe}$ ≈ 2, $R_{As\text{-}Fe}$ ≈ 3.33 Å; Table 2). Instead, the EXAFS fit required two As-Fe paths at $R_{As\text{-}Fe1}$ ≈ 3.44 ± 0.01 Å ($CN_{As\text{-}Fe1}$ ≈ 6) and $R_{As\text{-}Fe2}$ ≈ 3.63 ± 0.03 Å ($CN_{As\text{-}Fe1}$ ≈ 3). These EXAFS fit-derived distances for the As-Fe correlation in the MGT solids obtained after 720 h were more consistent with the values obtained for an As(V)-substituted MGT reference ($R_{As\text{-}Fe1}$ ≈ 3.47 ± 0.01 Å, $R_{As\text{-}Fe2}$ ≈ 3.66 ± 0.03 Å), although the determined CN values were slightly lower for the experimental sample (see Table 2).

View Article Online
DOI: 10.1039/D1EN00384D

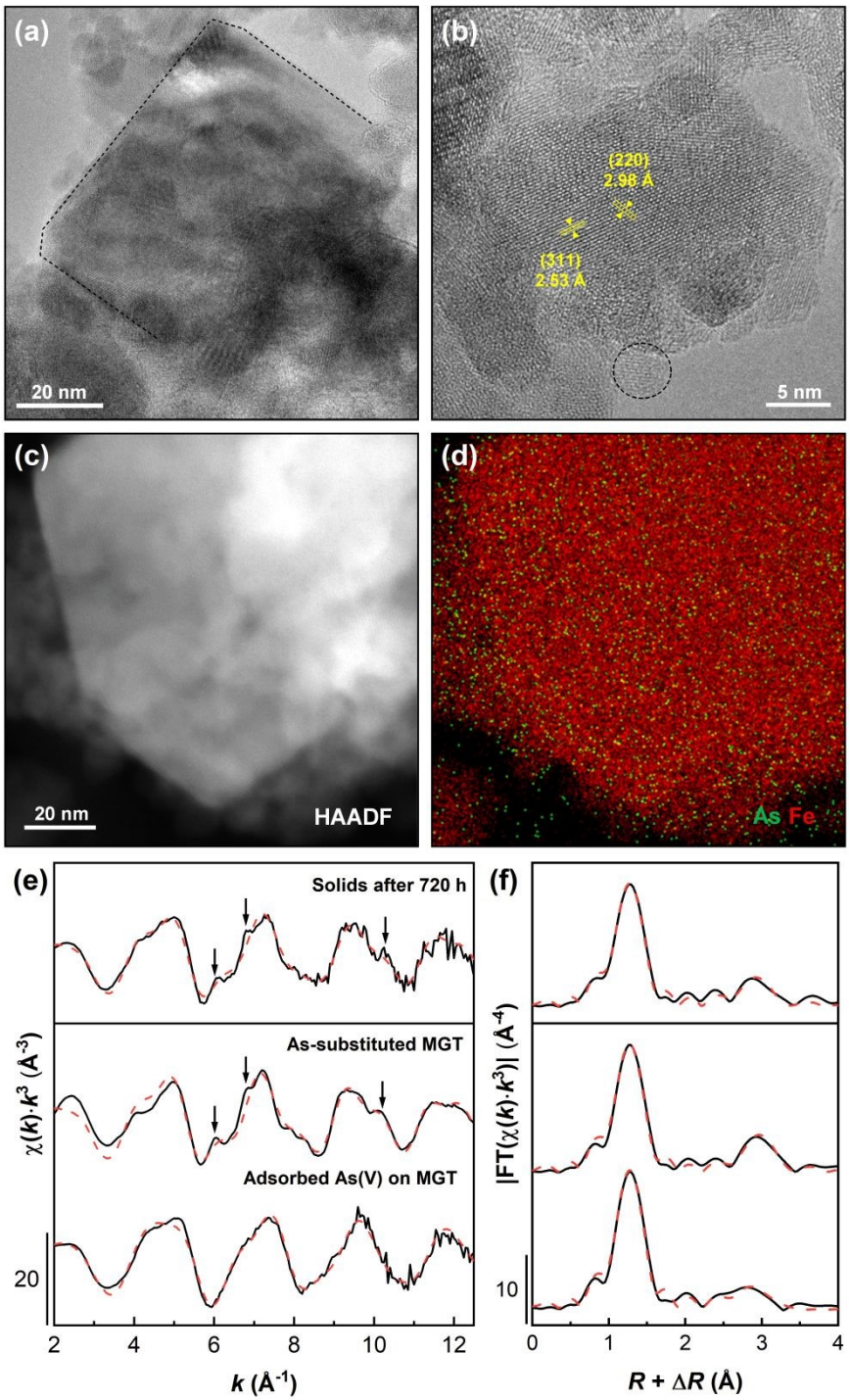

Figure 7. (a) TEM image of As(V)-reacted solids after 720 h showing the two distinct morphologies: (a) faceted nanocrystals (ca. 20-50 nm in diameter), with superimposed dotted outline added as a guide for the eye, and (b) rounded but smaller nanocrystals (ca. 5-10 nm in diameter). (c) HAADF-STEM overview of a faceted nanocrystal and the corresponding (d) combined EDX maps for Fe (red) and As (green). The As signal in (d) extends beyond the high contrast of the faceted crystal in (c) because As is also associated with the 2nd type of smaller rounder magnetite nanocrystals that surround it. (e) As K-edge EXAFS spectra of the 720-h reacted MGT solids compared to reference phases (van Genuchten et al.[33,40]): As-substituted MGT and As(V) adsorbed on MGT. (f) Fourier-transformed EXAFS spectra. The shell-by-shell fitting output (red dashed line) is superimposed on the experimental data (black solid line) and the shell-by-shell fitting results are given in Table 2.

View Article Online
DOI: 10.1039/D1EN00384D

Table 2. Shell-by-shell fitting results of the solids obtained after 720 h of the As(V)-bearing FHY transformation reaction, as well as As(V)-bearing MGT reference phases. Fitting parameters allowed to float are accompanied by fit-determined standard errors in parenthesis while constrained parameters appear without a parenthesis.

Sample	Atomic pairs	CN	R (Å)	σ^2 (Å^2)	ΔE_0 (eV)	R-factor
Solids after 720 h	As-O	4.1 (0.3)	1.70 (0.01)	0.003 (0.001)	5.3 (1.1)	0.015
	As-O-O	12	1.82(R_{As-O}) = 3.09	σ^2 (As-O)		
	As-Fe1	5.8 (1.1)	3.44 (0.01)	0.009		
	As-Fe2	3.2 (1.3)	3.63 (0.03)	σ^2 (As-Fe1)		
As References						
MGT, As(V) adsorbed	As-O	4.2 (0.4)	1.69 (0.01)	0.002 (0.001)	5.8 (1.3)	0.018
	As-O-O	12	1.82(R_{As-O}) = 3.08	σ^2 (As-O)		
	As-Fe	2.5 (1.6)	3.33 (0.02)	0.009 (0.005)		
MGT, As(V) substituted	As-O	4.3 (0.4)	1.70 (0.01)	0.003 (0.001)	4.9 (1.1)	0.015
	As-O-O	12	1.82(R_{As-O}) = 3.09	σ^2 (As-O)		
	As-Fe	7.6 (1.2)	3.47 (0.01)	0.009		
	As-Fe	3.9 (1.4)	3.66 (0.02)	σ^2 (As-Fe1)		

[a]CN, coordination number; R, interatomic distance; σ^2, mean-squared atomic displacement; and ΔE_0, change in threshold energy. The passive electron reduction factor (S_0^2) was fixed at 1.0. The multiple scattering As-O-O path was constrained geometrically to the single scattering As-O path (R_{As-O-O} = 1.82 R_{As-O}). All fits were carried out from 1 to 4 Å in R + ΔR - space. The number of independent points (N_{IDP}) in the fits was 18.9 and the number of variables (N_{Var}) was 6 to 8.

4. Discussion

4.1 Influence of As species on GR_{SO4} crystallization

Our results clearly show that the presence of As(III) and As(V) result in (1) delayed structural ordering during crystallization and (2) introduce localized disorder within the resulting GR_{SO4} crystals. First, adsorbed As onto FHY surface sites could have slowed down its dissolution,[27] thereby preventing the nucleation and growth of GR_{SO4}. It is well established that the transformation of FHY is initiated by the adsorption of Fe^{2+} on the FHY surface, followed by electron conduction through the FHY solid and subsequent release of dissolved Fe^{2+}.[21,42] This process creates "reactive surface sites" where FHY dissolves and recrystallizes to Fe (oxyhydr)oxides such as goethite or lepidocrocite at low [Fe^{2+}],[23] or GR or magnetite at high [Fe^{2+}].[24,26] As such, GR_{SO4} formed rapidly in our As-free experiments, and steadily increased in crystallinity and reached maximum crystallinity within 24 h because of the

sufficient supply of Fe^{2+} to induce FHY dissolution (~4 mM in excess relative to stoichiometric GR_{SO4}). In our As-amended experiments, however, As(III) or As(V) partially occupied the Fe^{2+} sorption sites in FHY, which could have delayed FHY dissolution and subsequent precipitation of GR_{SO4}.

Second, the dissolution of FHY in our As-amended experiments released As(III) or As(V) into solution which delayed GR_{SO4} crystallization and impacted the structural ordering and coherence of resulting particles. Our XRD (Figure 2) and TEM (Figures 4-6) observations suggest that GR_{SO4} crystal growth proceeds by Ostwald ripening,[43,44] wherein smaller nano-sized GR_{SO4} crystals re-crystallized to form the larger micron-sized hexagonal plates characteristic of GR_{SO4}.[19] We have shown in our recent work that both As(III) and As(V) adsorb at GR_{SO4} crystal edges in the ^2C geometry,[45] and can inhibit crystal dissolution. We therefore infer that the dissolution of the nano-sized GR_{SO4} crystals was delayed by the adsorbed As(III) or As(V). This also prevented further growth of the micron-sized crystals by inhibiting Fe-O-Fe polymers occupying the chain ends.[41,46] Although both As(III) and As(V) affected the GR_{SO4} crystallization, its structure and crystallinity, our results showed that the extent of these effects was dependent on the As oxidation state. The TEM images (Figure 4-6) revealed that As(III) greatly hindered structural ordering of the GR_{SO4} precipitates, taking at least eight times longer to reach maximum crystallinity observed compared to the As(V) system. These images also show that more GR_{SO4} nano-sized platelets remained in the As(III) system after 168 h compared to the As(V) system. We have shown in our previous study[19] that unlike to most Fe(III) (oxyhydr)xides,[18] As(III) has a strong sorption affinity for synthetic GR_{SO4} under near-neutral pH conditions. Hence, we argue that As(III) could form stable surface complexes at GR_{SO4} particle edges, which in turn inhibited the re-crystallization of the nano-sized platelets to the micron-sized plates. In addition to this, an earlier study by Thoral et al.[47] reported that dissolved As(III) can limit Fe polymerization and the crystallization of GR via Fe^{2+} oxidation. This supports our findings because there is significant As(III) release (up to ~14.3 µM) upon FHY dissolution (Figure 1c), resulting in the poorly crystalline initial As(III)-bearing GR_{SO4} precipitates observed after 0.25 h (Figure 1c). Moreover, increased crystallinity and structural ordering were only observed from the As(III)-GR_{SO4} precipitates by XRD and TEM once the initially released As(III)

had been adsorbed by the growing GR_{SO4} plates between 168 and 720 h (Figure 1c). Root et al.[2] reported a mixed-valence Fe(II)-Fe(III) phase, which has a local structure similar to GR, in high iron sediments enriched with As(III). The As(III)-bearing GR-type phase, formed from hydrous ferric oxides, also exhibited poor crystallinity, similar to what we have observed in our experiments. Our findings here could therefore have important implications on how mixed-valence Fe phases such as GR_{SO4} could limit the mobility of As(III), especially in As-affected regions in South and Southeast Asia[7] where groundwaters are characterized by reducing conditions[10] and dominated by As(III) instead of As(V).[14]

4.2 Phase stability of GR_{SO4} and its impact on As immobilization

GR is a metastable phase and thus transform to more thermodynamically stable Fe oxides such as MGT, under anoxic and circum-neutral to slightly alkaline pH conditions.[20,26] In our As-free experiments, MGT was first detected by XRD (Figure 2b) after 24 h of reaction, which also coincided with the substantial release of Fe^{2+} and SO_4^{2-} (Figure 1a and 1b) in the solution. As the reaction progressed, MGT continued to form in the system at the expense of GR_{SO4} until only MGT remained in the system after 720 h (Figure 2a, 2b and 3b). These observations are consistent with a transformation mechanism involving GR dissolution followed by MGT precipitation.[20,26]

Our solution chemistry (Figure 1) and XRD (Figure 2) data revealed that the presence of As in the system increased the stability of GR_{SO4} against transformation to MGT. The extent of this stabilizing effect was dependent on the As oxidation state, similar to the inhibitory role of As sorbed to the initial FHY on the GR_{SO4} crystallization discussed above. In the case of As(V), MGT was only identified by XRD in the solids after 168 h of reaction (Figure 2e and 2f), which was 7 times longer than in the As-free system. The precipitation of MGT was accompanied by dissolved Fe^{2+} and SO_4^{2-} release (Figure 1a and 1b), which further strengthens the idea that GR_{SO4} dissolution is needed in order for MGT to form. Complete conversion to MGT was observed only after 720 h in the As(V) system. Although GR_{SO4} fully transformed to MGT in the As(V)-amended experiments, As(V) was not re-released into solution (Figure 1c). Our combined STEM-EDX and As K-edge EXAFS data revealed that As(V) was

View Article Online
DOI: 10.1039/D1EN00384D

homogeneously distributed within the MGT precipitates, and structurally incorporated into its crystal structure (at least partially; Figure 7). The EXAFS-derived distances for the As-Fe correlations in MGT precipitates formed after 720 h suggest that $As^{V}O_4$ partially substituted for the $Fe^{III}O_4$ tetrahedral sites in the MGT crystal. This observation is consistent with the previously proposed mechanism of As(V) incorporation via Fe^{2+}-induced recrystallization of MGT,[33,48] which is also supported by formation of larger, faceted MGT nanoparticles (~20-50 nm) in our experiments.[49]

On the contrary, MGT did not form in the As(III) system over the monitored 720-h reaction; no MGT was observed by XRD in our analyses (Figure 2c and 2d), despite the fact that both $Fe^{2+}$and SO_4^{2-} were released in the solution between 360 and 720 h (Figure 1a and 1b). This release could indicate the onset of partial dissolution of As(III)-bearing GR_{SO4}, considering that the dissolved [Fe^{2+}] released in the solution (~1.6 mM) was comparable to that in the As(V) system (~1.4 mM) at the end of 720 h. However, it is also likely that the adsorbed As(III) at the GR_{SO4} particle edges (in binuclear ^2C geometry) inhibited substantial crystal dissolution, as documented in our previous work.[45] This inhibition and retardation of dissolution is likely the reason that prevented MGT precipitation in the As(III)-system even after 720 h (30 d). Overall, our results revealed that both As(III) and As(V) were efficiently sequestered by the transformation solids at the end of the 720-h experiment, either as surface complexes in the case of GR phases, or structurally incorporated in the MGT crystal structure. The importance of the above results to natural processes must however also take into consideration that As uptake and/or re-release is likely also to be affected by the more complex composition of natural groundwaters.

In natural subsurface environments, iron mineral transformations may take even longer due to the presence of other inorganic anions, e.g., dissolved silica (Si), phosphate (PO_4^{3-}), and organic ligands in the pore water or groundwater. For example, sorbed Si and PO_4^{3-} have been shown to inhibit GR transformation to other iron (oxyhydr)oxides.[50-52] In our previous study,[20] we have shown that synthetic GR_{SO4} aged in As-spiked natural groundwater (see Table 1) was stable for up to >120 d at 25 °C, with only trace amounts of MGT forming in the system. Its solid phase stability was further

enhanced when As-bearing GR_{SO4} was aged at 4 °C as seen from the absence of MGT even after 424 d (> 1 yr). Combining these with the results of this work, we clearly showed that As-bearing GR phases could remain stable in natural environments over extended periods of time. This can minimize the risk of As remobilization in contaminated environments, as shown for example in As sequestered by naturally occurring GR found in high iron sediments and mine drainage systems.[2,4] In addition to natural settings, GR phases also often form as corrosion or transformation products of zero-valent iron nanoparticles used for *in situ* groundwater remediation technologies,[53,54] and previous studies have shown that As was strongly partitioned onto the resulting GR phases.[55,56] More importantly, if these As-bearing GR phases eventually transform to MGT, we do not expect significant As release as we have shown in our current work and in earlier studies.[32,33]

5. Conclusions

GR phases have been reported to have high As sorption capacities, yet their occurrence, formation and long-term stability in As-contaminated subsurface environments are still poorly understood. In this study, we investigated GR_{SO4} formation via the Fe^{2+}-catalyzed transformation of FHY in the presence of As(III) or As(V), as well as its subsequent transformation to MGT. We found that As(III) has a stronger inhibitory effect on GR_{SO4} crystallization (at least eight-fold) and transformation rates compared to As(V), with the As(III)-bearing GR_{SO4} stable up to 720 h (30 d). Our results also revealed that As(III) can also inhibit structural ordering during GR_{SO4} crystallization, as evidenced by the formation of poorly crystalline nano-sized platelets and non-coherent crystal structure of the very thin micron-sized hexagonal plates. Both As(III) and As(V) were effectively immobilized by GR_{SO4} and MGT particles, respectively, at the end of 720 h, although As(III) was initially released in the early stages of GR_{SO4} crystallization. Overall, these results revealed new insights on GR_{SO4} crystallization and transformation in the presence of As, as well as the structure and morphology of the As-bearing GR_{SO4}. More

importantly, these results further highlight the potential of GR phases in controlling As mobility in contaminated environments, especially in reduced groundwater where As(III) dominates over As(V).

Conflicts of Interest

There are no conflicts of interests to declare.

Acknowledgements

This project has received funding from the European Union's Horizon 2020 Marie Skłodowska-Curie Innovative Training Network Grant No. 675219, and the Helmholtz Recruiting Initiative (Award no. I-044-16-01) awarded to L.G.B. All ICP-OES analyses were carried out at the Helmholtz Laboratory for the Geochemistry of the Earth Surface (HELGES) at GFZ Potsdam. TEM access was possible through the Royal Society of Chemistry (RSC) Researcher Mobility Grant (Project no. RM1602-226) and Geo.X Travel Grant (Grant No. SO_087_GeoX) awarded to J.P.H.P., and the EPSRC grant EP/M028143/1 at the Leeds Electron Microscopy and Spectroscopy Centre (LEMAS) at University of Leeds. The authors acknowledge the European Synchrotron Radiation Facility (ESRF) for the provision of synchrotron radiation facilities (experiment no. EV-338) and we would like to thank Sakura Pascarelli for assistance in using beamline BM23. J.P.H.P. is very grateful to the NanoGeoScience group at University of Copenhagen, and the LEMAS and Cohen Geochemistry groups at University of Leeds for being kind hosts during his research visits; special thanks go to Marco Mangayayam, Marcel Ceccato, Andrew Connelly and Andrew Hobson for all their help in the experiments.

References

1. M. Usman, J. M. Byrne, A. Chaudhary, S. Orsetti, K. Hanna, C. Ruby, A. Kappler and S. B. Haderlein, Magnetite and green rust: Synthesis, properties, and environmental applications of mixed-valent iron minerals, *Chem. Rev.*, 2018, **118**, 3251-3304.

2. R. A. Root, S. Dixit, K. M. Campbell, A. D. Jew, J. G. Hering and P. A. O'Day, Arsenic sequestration by sorption processes in high-iron sediments, *Geochim. Cosmochim. Acta*, 2007, **71**, 5782-5803.
3. E. Dore, D. Fancello, N. Rigonat, D. Medas, R. Cidu, S. Da Pelo, F. Frau, P. Lattanzi, P. A. Marras, C. Meneghini, F. Podda, V. Rimondi, R. L. Runkel, B. Kimball, R. B. Wanty and G. De Giudici, Natural attenuation can lead to environmental resilience in mine environment, *Appl. Geochem.*, 2020, **117**, 104597.
4. C. A. Johnson, G. Freyer, M. Fabisch, M. A. Caraballo, K. Kusel and M. F. Hochella, Observations and assessment of iron oxide and green rust nanoparticles in metal-polluted mine drainage within a steep redox gradient, *Environ. Chem.*, 2014, **11**, 377-391.
5. C. A. Johnson, M. Murayama, K. Kusel and M. F. Hochella, Polycrystallinity of green rust minerals and their synthetic analogs: Implications for particle formation and reactivity in complex systems, *Am. Mineral.*, 2015, **100**, 2091-2105.
6. J. M. Bearcock, W. T. Perkins and N. J. Pearce, Laboratory studies using naturally occurring "green rust" to aid metal mine water remediation, *J. Hazard. Mater.*, 2011, **190**, 466-473.
7. P. L. Smedley and D. G. Kinniburgh, A review of the source, behaviour and distribution of arsenic in natural waters, *Appl. Geochem.*, 2002, **17**, 517-568.
8. D. J. Vaughan, Arsenic, *Elements*, 2006, **2**, 71-75.
9. J. Podgorski and M. Berg, Global threat of arsenic in groundwater, *Science*, 2020, **368**, 845-850.
10. M. Amini, K. C. Abbaspour, M. Berg, L. Winkel, S. J. Hug, E. Hoehn, H. Yang and C. A. Johnson, Statistical modeling of global geogenic arsenic contamination in groundwater, *Environ. Sci. Technol.*, 2008, **42**, 3669-3675.
11. M. Berg, H. C. Tran, T. C. Nguyen, H. V. Pham, R. Schertenleib and W. Giger, Arsenic contamination of groundwater and drinking water in Vietnam: a human health threat, *Environ. Sci. Technol.*, 2001, **35**, 2621-2626.
12. S. Fendorf, H. A. Michael and A. van Geen, Spatial and temporal variations of groundwater arsenic in South and Southeast Asia, *Science*, 2010, **328**, 1123-1127.
13. World Health Organization, Guidelines for drinking-water quality: Fourth edition incorporating the first addendum, 2017.
14. P. H. Masscheleyn, R. D. Delaune and W. H. Patrick, Arsenic and selenium chemistry as affected by sediment redox potential and pH, *J. Environ. Qual.*, 1991, **20**, 522-527.
15. S. Dixit and J. G. Hering, Comparison of arsenic(V) and arsenic(III) sorption onto iron oxide minerals: Implications for arsenic mobility, *Environ. Sci. Technol.*, 2003, **37**, 4182-4189.
16. R. J. Bowell, Sorption of arsenic by iron oxides and oxyhydroxides in soils, *Appl. Geochem.*, 1994, **9**, 279-286.

17. B. A. Manning, S. E. Fendorf and S. Goldberg, Surface structures and stability of arsenic(III) on goethite: Spectroscopic evidence for inner-sphere complexes, *Environ. Sci. Technol.*, 1998, **32**, 2383-2388.
18. L. C. Roberts, S. J. Hug, T. Ruettimann, M. Billah, A. W. Khan and M. T. Rahman, Arsenic removal with iron(II) and iron(III) in waters with high silicate and phosphate concentrations, *Environ. Sci. Technol.*, 2004, **38**, 307-315.
19. J. P. H. Perez, H. M. Freeman, J. A. Schuessler and L. G. Benning, The interfacial reactivity of arsenic species with green rust sulfate (GR_{SO4}), *Sci. Total Environ.*, 2019, **648**, 1161-1170.
20. J. P. H. Perez, A. A. Schiefler, S. N. Rubio, M. Reischer, N. D. Overheu, L. G. Benning and D. J. Tobler, Arsenic removal from natural groundwater using 'green rust': Solid phase stability and contaminant fate, *J. Hazard. Mater.*, 2021, **401**, 123327.
21. C. A. Gorski and M. M. Scherer, Fe^{2+} sorption at the Fe oxide-water interface: A revised conceptual framework, in *Aquatic Redox Chemistry*, eds. P. G. Tratnyek, T. J. Grundl and S. B. Haderlein, American Chemical Society, 2011, vol. 1071, ch. 15, pp. 315-343.
22. E. D. Melton, E. D. Swanner, S. Behrens, C. Schmidt and A. Kappler, The interplay of microbially mediated and abiotic reactions in the biogeochemical Fe cycle, *Nat. Rev. Microbiol.*, 2014, **12**, 797-808.
23. D. D. Boland, R. N. Collins, C. J. Miller, C. J. Glover and T. D. Waite, Effect of solution and solid-phase conditions on the Fe(II)-accelerated transformation of ferrihydrite to lepidocrocite and goethite, *Environ. Sci. Technol.*, 2014, **48**, 5477-5485.
24. C. M. Hansel, S. G. Benner and S. Fendorf, Competing Fe (II)-induced mineralization pathways of ferrihydrite, *Environ. Sci. Technol.*, 2005, **39**, 7147-7153.
25. M. Usman, K. Hanna, M. Abdelmoula, A. Zegeye, P. Faure and C. Ruby, Formation of green rust via mineralogical transformation of ferric oxides (ferrihydrite, goethite and hematite), *Appl. Clay Sci.*, 2012, **64**, 38-43.
26. A. Sumoondur, S. Shaw, I. Ahmed and L. G. Benning, Green rust as a precursor for magnetite: An in situ synchrotron based study, *Mineral. Mag.*, 2008, **72**, 201-204.
27. H. D. Pedersen, D. Postma and R. Jakobsen, Release of arsenic associated with the reduction and transformation of iron oxides, *Geochim. Cosmochim. Acta*, 2006, **70**, 4116-4129.
28. Y. Masue-Slowey, R. H. Loeppert and S. Fendorf, Alteration of ferrihydrite reductive dissolution and transformation by adsorbed As and structural Al: Implications for As retention, *Geochim. Cosmochim. Acta*, 2011, **75**, 870-886.
29. J. P. H. Perez, D. J. Tobler, A. N. Thomas, H. M. Freeman, K. Dideriksen, J. Radnik and L. G. Benning, Adsorption and reduction of arsenate during the Fe^{2+}-induced transformation of ferrihydrite, *ACS Earth Space Chem.*, 2019, **3**, 884-894.

30. A. Géhin, C. Ruby, M. Abdelmoula, O. Benali, J. Ghanbaja, P. Refait and J.-M. R. Génin, Synthesis of Fe(II-III) hydroxysulphate green rust by coprecipitation, *Solid State Sci.*, 2002, **4**, 61-66.
31. B. C. Christiansen, T. Balic-Zunic, P. O. Petit, C. Frandsen, S. Morup, H. Geckeis, A. Katerinopoulou and S. L. S. Stipp, Composition and structure of an iron-bearing, layered double hydroxide (LDH) - Green rust sodium sulphate, *Geochim. Cosmochim. Acta*, 2009, **73**, 3579-3592.
32. Y. Wang, G. Morin, G. Ona-Nguema and G. E. Brown, Jr., Arsenic(III) and arsenic(V) speciation during transformation of lepidocrocite to magnetite, *Environ. Sci. Technol.*, 2014, **48**, 14282-14290.
33. C. M. van Genuchten, T. Behrends and K. Dideriksen, Emerging investigator series: Interdependency of green rust transformation and the partitioning and binding mode of arsenic, *Environ. Sci. Process Impacts*, 2019, **21**, 1459-1476.
34. I. A. Ahmed, L. G. Benning, G. Kakonyi, A. D. Sumoondur, N. J. Terrill and S. Shaw, Formation of green rust sulfate: A combined in situ time-resolved X-ray scattering and electrochemical study, *Langmuir*, 2010, **26**, 6593-6603.
35. R. M. Cornell and U. Schwertmann, *The Iron Oxides: Structure, Properties, Reactions, Occurrences and Uses*, Wiley-VCH Verlag GmbH & Co. KGaA, Weinheim, FRG, 2nd edn., 2003.
36. J. D. Rodriguez-Blanco, S. Shaw and L. G. Benning, The kinetics and mechanisms of amorphous calcium carbonate (ACC) crystallization to calcite, viavaterite, *Nanoscale*, 2011, **3**, 265-271.
37. N. Hondow, R. Brydson, P. Wang, M. D. Holton, M. R. Brown, P. Rees, H. D. Summers and A. Brown, Quantitative characterization of nanoparticle agglomeration within biological media, *Journal of Nanoparticle Research*, 2012, **14**, 977.
38. O. Mathon, A. Beteva, J. Borrel, D. Bugnazet, S. Gatla, R. Hino, I. Kantor, T. Mairs, M. Munoz, S. Pasternak, F. Perrin and S. Pascarelli, The time-resolved and extreme conditions XAS (TEXAS) facility at the European Synchrotron Radiation Facility: The general-purpose EXAFS bending-magnet beamline BM23, *J. Synchr. Radiat.*, 2015, **22**, 1548-1554.
39. S. M. Webb, SIXpack: a graphical user interface for XAS analysis using IFEFFIT, *Phys. Scr.*, 2005, **T115**, 1011-1014.
40. C. M. van Genuchten, T. Behrends, S. L. S. Stipp and K. Dideriksen, Achieving arsenic concentrations of <1 µg/L by Fe(0) electrolysis: The exceptional performance of magnetite, *Water Res.*, 2020, **168**, 115170.
41. G. A. Waychunas, B. A. Rea, C. C. Fuller and J. A. Davis, Surface chemistry of ferrihydrite: Part 1. EXAFS studies of the geometry of coprecipitated and adsorbed arsenate, *Geochim. Cosmochim. Acta*, 1993, **57**, 2251-2269.
42. J. E. Katz, X. Zhang, K. Attenkofer, K. W. Chapman, C. Frandsen, P. Zarzycki, K. M. Rosso, R. W. Falcone, G. A. Waychunas and B. Gilbert, Electron small polarons and their mobility in iron (oxyhydr)oxide nanoparticles, *Science*, 2012, **337**, 1200-1203.

43. W. Ostwald, Studien über die Bildung und Umwandlung fester Körper, *Z. Phys. Chem.*, 1897, **22**, 289-330.
44. R. Guilbaud, M. L. White and S. W. Poulton, Surface charge and growth of sulphate and carbonate green rust in aqueous media, *Geochim. Cosmochim. Acta*, 2013, **108**, 141-153.
45. J. P. H. Perez, H. M. Freeman, A. P. Brown, C. M. van Genuchten, K. Dideriksen, M. S'Ari, D. J. Tobler and L. G. Benning, Direct visualization of arsenic binding on green rust sulfate, *Environ. Sci. Technol.*, 2020, **54**, 3297-3305.
46. W. R. Richmond, M. Loan, J. Morton and G. M. Parkinson, Arsenic removal from aqueous solution via ferrihydrite crystallization control, *Environ. Sci. Technol.*, 2004, **38**, 2368-2372.
47. S. Thoral, J. Rose, J. M. Garnier, A. van Geen, P. Refait, A. Traverse, E. Fonda, D. Nahon and J. Y. Bottero, XAS Study of iron and arsenic speciation during Fe(II) oxidation in the presence of As(III), *Environ. Sci. Technol.*, 2005, **39**, 9478-9485.
48. B. L. Huhmann, A. Neumann, M. I. Boyanov, K. M. Kemner and M. M. Scherer, Emerging investigator series: As(v) in magnetite: incorporation and redistribution, *Environ. Sci. Process Impacts*, 2017, **19**, 1208-1219.
49. J. J. M. Lenders, G. Mirabello and N. Sommerdijk, Bioinspired magnetite synthesis via solid precursor phases, *Chem. Sci.*, 2016, **7**, 5624-5634.
50. S. K. Kwon, K. Kimijima, K. Kanie, S. Suzuki, A. Muramatsu, M. Saito, K. Shinoda and Y. Waseda, Influence of silicate ions on the formation of goethite from green rust in aqueous solution, *Corros. Sci.*, 2007, **49**, 2946-2961.
51. O. Benali, M. Abdelmoula, P. Refait and J. M. R. Genin, Effect of orthophosphate on the oxidation products of Fe(II)-Fe(III) hydroxycarbonate: The transformation of green rust to ferrihydrite, *Geochim. Cosmochim. Acta*, 2001, **65**, 1715-1726.
52. F. Bocher, A. Gehin, C. Ruby, J. Ghanbaja, M. Abdelmoula and J. M. R. Genin, Coprecipitation of Fe(II-III) hydroxycarbonate green rust stabilised by phosphate adsorption, *Solid State Sci.*, 2004, **6**, 117-124.
53. Y. Furukawa, J.-w. Kim, J. Watkins and R. T. Wilkin, Formation of Ferrihydrite and Associated Iron Corrosion Products in Permeable Reactive Barriers of Zero-Valent Iron, *Environ. Sci. Technol.*, 2002, **36**, 5469-5475.
54. M. C. Mangayayam, J. P. H. Perez, K. Dideriksen, H. M. Freeman, N. Bovet, L. G. Benning and D. J. Tobler, Structural transformation of sulfidized zerovalent iron and its impact on long-term reactivity, *Environ. Sci.: Nano*, 2019, **6**, 3422-3430.
55. C. Su and R. W. Puls, Significance of iron(II,III) hydroxycarbonate green rust in arsenic remediation using zerovalent iron in laboratory column tests, *Environ. Sci. Technol.*, 2004, **38**, 5224-5231.

56. C. Su and R. W. Puls, In Situ Remediation of Arsenic in Simulated Groundwater Using Zerovalent Iron: Laboratory Column Tests on Combined Effects of Phosphate and Silicate, *Environ. Sci. Technol.*, 2003, **37**, 2582-2587.

57. H. M. Anawar, J. Akai and H. Sakugawa, Mobilization of arsenic from subsurface sediments by effect of bicarbonate ions in groundwater, *Chemosphere*, 2004, **54**, 753-762.

58. N. Mladenov, Y. Zheng, B. Simone, T. M. Bilinski, D. M. McKnight, D. Nemergut, K. A. Radloff, M. M. Rahman and K. M. Ahmed, Dissolved organic matter quality in a shallow aquifer of Bangladesh: Implications for arsenic mobility, *Environ. Sci. Technol.*, 2015, **49**, 10815-10824.